Available online at www.sciencedirect.com
ScienceDirect
Journal of Power Sources 160 (2006) 1195–1203
JOURNAL OF POWER SOURCES
www.elsevier.com/locate/jpowsour

Quantification of liquid water accumulation and distribution in a polymer electrolyte fuel cell using neutron imaging

A. Turhan, K. Heller, J.S. Brenizer, M.M. Mench *

Fuel Cell Dynamics and Diagnostics Laboratory, Radiation Science and Engineering Center, and Department of Mechanical and Nuclear Engineering, The Pennsylvania State University, University Park, PA 16802, United States

Received 27 January 2006; received in revised form 9 March 2006; accepted 10 March 2006
Available online 27 April 2006

Abstract

Operating parameters, material properties and flow field geometry have a deterministic role on the water storage and distribution within the flow channels and porous media in a fuel cell. However, their effects are not yet precisely understood. In this study, extensive neutron imaging experiments were conducted to visualize and quantify the amount of liquid water in the fuel cell channels and diffusion media as a function of inlet gas flow rate, cell pressure and inlet relative humidity. A seven-channel parallel flow configuration PEFC was used to isolate these parameters from flow field switchback interaction effects.

The neutron imaging experiments were performed at different inlet gas flow rates, operating cell pressures and inlet relative humidities. At each operating condition, the distribution of liquid water in the diffusion media under the lands, and in or under the channels was obtained. Furthermore, at three different cell pressures (0.2 MPa, 0.15 MPa and 0.1 MPa), liquid water distribution and quantification was obtained. The liquid water mass in the cell decreased with increasing pressure for over-humidified anode inlet conditions. Comparison of the fuel cell performance with the total liquid water mass in the cell indicates a non-monotonic relationship between liquid water content and performance. Furthermore, cell performance was highly sensitive to incremental changes in the membrane liquid water content.

Keywords: Flooding; Polymer electrolyte fuel cell; Solid polymer electrolyte; Neutron imaging; Water storage; Residual water

1. Introduction

The hydrogen polymer electrolyte fuel cell (PEFC) is an electrochemical device which converts the chemical energy of a fuel and oxidizer into electrical energy, and generates water at the cathode. There is a complex relationship between moisture content and performance in PEFCs. The ionic conductivity of Nafion® and related perfluorinated sulfonic polymers is suitable when fully hydrated, but decreases sharply with lowered membrane water content [1–5]. However, if excessive liquid water forms in the cell, it can cover the surface of the catalyst layers, fill the pores of the gas diffusion layer (GDL), or block the flow channels and increase parasitic pressure losses. Each variety of liquid blockage ultimately prevents the diffusion of reactant gases into the reaction sites. This phenomenon is known as 'flooding' which can drastically decrease PEFC performance. Due to the delicate balance between the benefit of a fully humidified electrolyte and the deleterious effects of flooding concomitant with liquid water accumulation, there is extensive ongoing research to more fundamentally understand two-phase water transport in PEFCs and enable performance and design optimization. Additionally, the factors governing liquid water storage in the diffusion media under normal operation are becoming an increasingly important topic as system transients, degradation, and freeze–thaw behavior become a greater focus for developers.

Incidence of flooding depends on several intercoupled phenomena such as heat transfer, fluid mechanics, electrochemistry, thermodynamic processes, materials, operating parameters and cell geometry. There have been numerous attempts to model two-phase flow and flooding [6–20]. However, these models are often validated using bulk polarization curves, which can be misleading since performance behavior at high current density can be similar for both the flooding and dry-out conditions [21].

* Corresponding author. Tel.: +1 814 865 0060; fax: +1 814 863 4848.
E-mail addresses: mmench@psu.edu, mmm124@psu.edu (M.M. Mench).

0378-7753/$ – see front matter © 2006 Elsevier B.V. All rights reserved.
doi:10.1016/j.jpowsour.2006.03.027

Nomenclature

A	channel cross sectional area (m^2)
b	half width of the channel (m)
B	total width of the channel (m)
c	chord length of droplet (m)
d_c	hydraulic diameter of the channel (m)
F	force (N)
h	droplet height (m)
MW	molecular weight ($g\,mol^{-1}$)
P	pressure (Pa)
P_a	pressure at AA′ (Pa)
P_b	pressure at BB′ (Pa)
Re	Reynolds number
RH	relative humidity
m	mass (kg)
$\dot{m}$	mass flow rate ($kg\,s^{-1}$)
$\dot{n}$	molar flow rate ($mol\,s^{-1}$)
T	temperature (K)
U	velocity ($m\,s^{-1}$)

Greek symbols

δ	thickness (m)
Δ	difference between advancing and receding angle (rad)
$\gamma_{sl}, \gamma_{sv}, \gamma_{lv}$	interfacial tension (solid–liquid, solid–vapor, liquid–vapor) ($N\,m^{-1}$)
μ	fluid viscosity ($kg\,m^{-1}\,s^{-1}$)
θ	solid/liquid-phase contact angle (rad)
ρ	density ($kg\,m^{-3}$)

Subscripts

A	advancing
air	air
cell	fuel cell
drag	drag
el	electrolyte
H_2	hydrogen
H_2O	water
in	inlet
mix	mixture
R	receding
sat	saturation

Superscripts

dry	dry, zero humidity
sat	saturated

Hence, it is necessary to obtain greater spatial resolution in the data to enable model validation and to gain a thorough understanding of two-phase phenomena. One available tool to provide this information is neutron imaging.

There has been a relative paucity of research in experimental visualization and quantification of the liquid water distribution [22–26]. Recently, neutron imaging has demonstrated the capability to directly observe and quantify liquid water content in the flow channels and diffusion media of operating fuel cells [27–31]. Neutron imaging is an excellent non-intrusive technique for visualization of the two-phase flow within the fuel cell, in either dynamic or steady-state operation. The Penn State Breazeale Neutron Imaging for Fuel Cells Laboratory has developed the technology to accurately quantify the liquid water in the fuel cell.

2. Experimental

In order to utilize the neutron imaging technique on the fuel cells, the neutron radioscopy system at Penn State Radiation Science and Engineering Center was used. The tests were performed on a fuel cell diagnostic system, shown in Fig. 1, and neutron images were processed with an in-house image processing software and hardware. The details of the storage and presentation of the collected images were described in a previous publication [31]. The fuel cell temperature was monitored from the cathode backing plate. Two 6.3 mm diameter cartridge heaters, one in each fuel cell backing plate below the active area, provided heat, while small fans operated to convectively remove excess heat.

A 14.5 cm^2 active area fuel cell with 200 μm, 75% porous diffusion media and 40 μm thick Nafion® membrane was used in all experiments. The anode and cathode flow channels are aligned in parallel. The flow field is constructed of gold plated aluminum with parallel channels, sealed to prevent absorption of water. The channel width is 1 mm and channel height is 0.5 mm. Effects of three different operation parameters: (1) inlet relative humidity, (2) cell pressure and (3) gas flow rate, were investigated in the experiments. Tests were performed at three different pressures, four different flow rates and four different inlet

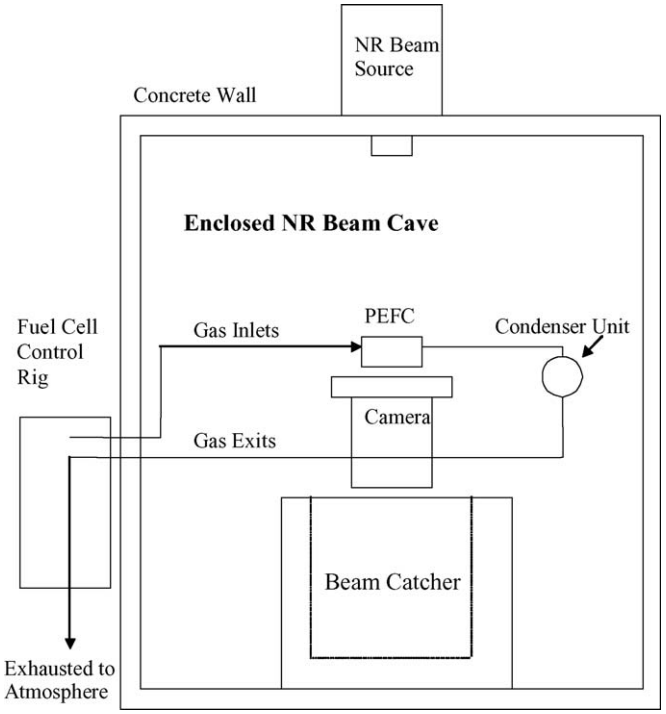

Fig. 1. Experimental setup. The fuel cell is positioned in front of the camera, and the anode and cathode inlet lines are insulated.

Table 1
Test matrix

Condition	T_{cell} (°C)	Pressure (MPa)	Stoic. (at 1 A cm^{-2})	Flow rate anode (cm^3 min^{-1})	Flow rate cathode (cm^3 min^{-1})	Anode, $T_{bubbler}$ (°C)	Cathode, $T_{bubbler}$ (°C)
1	80	0.2	1.5/1.5	149	356	90	80
2	80	0.2	2/2	199	475	90	80
3	80	0.2	3/3	299	712	90	80
4	80	0.2	5/5	497	1188	90	80
5	80	0.2	1.5/1.5	149	356	90	Non-humidified
6	80	0.2	2/2	199	475	90	Non-humidified
7	80	0.2	3/3	299	712	90	Non-humidified
8	80	0.2	5/5	497	1188	90	Non-humidified
9	80	0.15	1.5/1.5	149	356	90	80
10	80	0.15	3/3	299	712	90	80
11	80	0.15	10/10	993	2376	90	80
12	80	0.1	1.5/1.5	149	356	90	80
13	80	0.1	3/3	299	712	90	80
14	80	0.1	10/10	993	2376	90	80
15	80	0.2	3/3	299	712	50	50
16	80	0.2	2/2	199	475	50	50
17	80	0.2	1.5/1.5	149	356	50	50
18	80	0.2	3/3	299	712	60	60
19	80	0.2	2/2	199	475	60	60
20	80	0.2	1.5/1.5	149	356	60	60
21	80	0.2	3/3	299	712	70	70
22	80	0.2	2/2	199	475	70	70
23	80	0.2	1.5/1.5	149	356	70	70

relative humidity values. The details of the test matrix are presented in Table 1.

2.1. Data acquisition and analysis

A video capturing software program, Streampix, collects and records the fully digital video signal produced by the CCD camera system on a customized computer. The systems temporal and spatial resolution is 30 frames s^{-1} and 129 μm pixel^{-1} in the 14.5 cm^2 active area of the cell. At this frame rate digital radioscopic images can be recorded for up to 45 min. The image stacks are stored on a date-based directory structure with each stack file name containing a descriptor of the experiment recorded. These features allow single images of interest or multiple sequential images to be easily located and analyzed.

2.2. Image post-processing and water quantification

Several post-process image enhancement techniques and water quantification processes were used to increase the overall image quality and accuracy of the water quantification process as described in detail in reference [31]. A brief summary of these techniques will be given here.

The determination of water content within the cell as a function of time is attainable by referencing a pre-generated calibration look-up table which correlates water thickness to pixel luminance. This look-up table is generated using a water-filled wedge, constructed of aluminum. The wedge contains a water-filled void of continuously varying thickness. Through statistical analysis of the wedge image, pixel luminance values are recorded at the known water thickness levels, producing a calibration table that can be referenced to assign water thickness values to areas within the cell. Note that the effect of temperature of the wedge on water density was calculated to be negligible in our operation range. The mass and volume of water in the cell can then be computed for finite instances or as a varying function of time. A total of 60 images (5 frames s^{-1} for 12 s) were taken for each steady-state fuel cell condition. All 60 frames were averaged together into a single image to reduce instrument noise and pixel variance. In such an image, the water-filled wedge's grayscale pixel value versus height was plotted. This plot suggests a theoretical minimum water thickness of 10 μm is observable with the imaging system. Subsequent experiments with in-house constructed water channel calibration channels show that the current observable limit of liquid water is at most 12.7 μm. That is, liquid water thicknesses (e.g. total accumulated liquid water in the line-of-sight of the neutron beam including anode and cathode) less than 12.7 μm are below the current detectability limit of the imaging system and will not be detected. In addition to total water mass calculation, the liquid water under the landings and in, or under, the channels is also calculated using a masking technique. Digital masks were generated to delineate between the channel and landings. Once these masks were generated, they were applied to images of the cell taken during normal operation, which were then quantified for water mass content. The results were water mass values and colorized images for either the channel or landing areas only.

3. Results and discussion

3.1. Gas flow rate effect

Several neutron imaging tests were performed at different inlet gas flow rate conditions in order to observe the effect of

Table 2
Calculated liquid water mass values

Test condition	Cathode flow (sccm)	Liquid water (mg)		
		Channel	Landing	Total
1	356	58.1	64.7	122.8
2	475	74.0	81.6	155.6
3	712	45.0	56.4	101.4
4	1188	46.1	60.5	106.6
5	356	64.7	65.4	130.1
6	475	64.0	67.6	131.6
7	712	51.7	55.3	107.0
8	1188	41.5	51.5	93.0
9	356	67.3	74.6	141.9
10	712	43.3	58.1	101.4
11	2376	62.6	77.7	140.3
12	356	79.1	83.8	162.9
13	712	73.1	87.4	160.5
14	2356	66.2	76.4	142.6
15	712	33.7	45.8	79.5
16	475	30.0	40.0	70.0
17	356	33.1	43.2	76.3
18	712	29.2	39.0	68.2
19	475	31.8	41.9	73.7
20	356	28.9	38.0	66.9
21	712	32.9	44.1	77.0
22	475	30.3	39.3	65.6
23	356	30.9	40.2	71.1

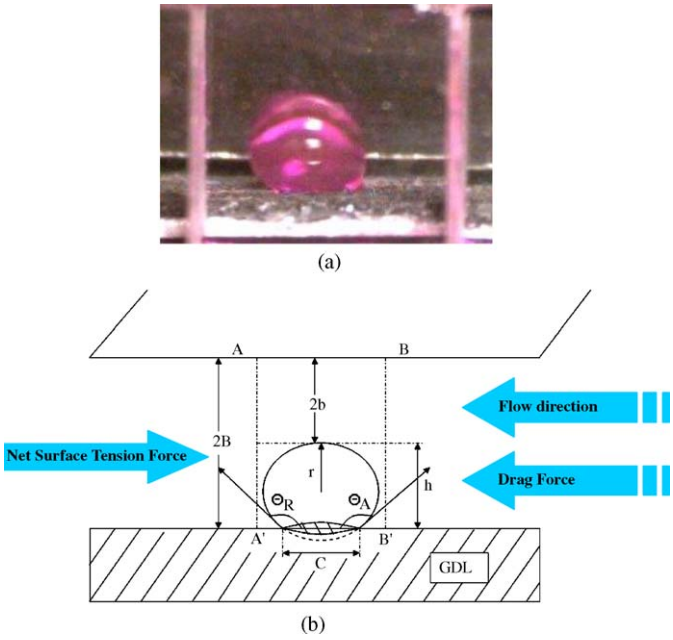

Fig. 3. (a) Picture of water droplet under the effect of reactant gas flow and (b) corresponding schematic drawing of force balance. The shape of the droplet is distorted due to the shear effect. The advancing (θ_A) and receding (θ_R) shear angles are shown in the schematic from Kumbur et al. [26].

flow rate on liquid water accumulation in the fuel cell. At each test condition, the cell voltage data were also taken so that cross comparison of water accumulation and cell performance could be made. Experiments were performed at constant current density (0.35 A cm^{-2}). The calculated liquid water values at each condition are summarized in Table 2.

In Fig. 2, the neutron images of Condition 2, 4 and 8 (Table 1) are shown. All the images are also available in color at www.mne.psu.edu/neutron2.pdf. At the low flow rate, fully humidified condition (Condition 2), a significant amount of channel liquid water accumulation was observed (light blue/green colored regions), and the observed motion of the liquid was from right to left, indicating channel water was formed mostly in cathode side. This is an expected result, since water generation is at the cathode catalyst and therefore there is a higher potential for the cathode side to flood. The amount of water in the cell was calculated as 155 mg. On the contrary, from the high flow rate, fully humidified condition (Condition 4), it can easily be seen that the channel level liquid water accumulation is almost entirely diminished due to the high inlet gas flow rates. All of the water appears in dark blue color, and increases toward cathode exit. Consequently, the total water mass in the cell decreased significantly (~30%), to 106 mg, due to the shear effect of the flow. In Condition 8, the image of high flow rate, dry inlet humidity condition shows the effect of flow rate on water management in the fuel cell at zero inlet humidity. The effect of

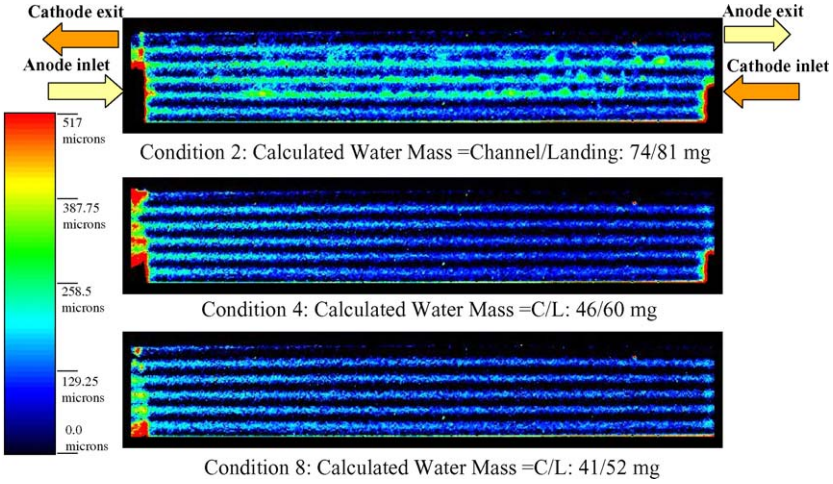

Fig. 2. Neutron images and total liquid water mass for the high and low flow rate over-humidifier inlet Conditions 2 and 4 of Table 1. Current density at all conditions is 0.35 A cm^{-2}.

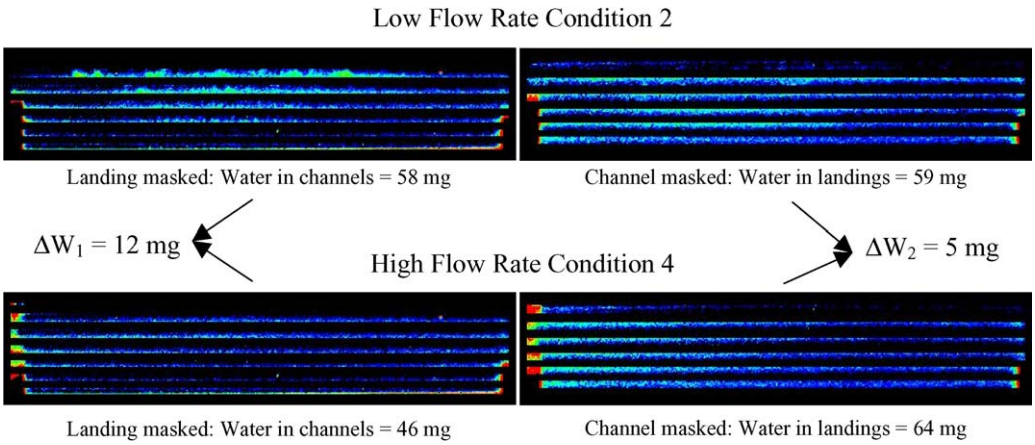

Fig. 4. Masked images for low flow rate Case #2 (upper two images) and high flow rate Case #4 (lower two images). There is more water accumulated under the landings than in or under the channels. The change in liquid water content, ΔW, is greater for the channels for increased flow rate case, although liquid under the land is also reduced with increasing channel flow.

non-humidified flow is apparent from the image, as total water mass in the cell reached a minimum of 93 mg, and almost all of the channel water has disappeared.

In order to explain the effect of flow rate effect on the water accumulation a theoretical model was developed by Kumbur et al. [26]. A detailed theoretical model of the influence of engineering parameters and operational parameters, including the channel level was studied. A macroscopic force balance was applied to find the functional dependence of the velocity of air on drag force. The final force balance is shown in Eq. (1). The shear effect on the water droplet is also illustrated in Fig. 3.

$$F_{P_x} + F_{\text{shear}_x} + F_{\text{drag}_x} = 0, \text{ where}$$

$$F_{\text{drag}_x} = -F_{\text{ST}_x}\frac{24\cdot\mu\cdot B^2\cdot U\cdot h^2}{\left(B-\frac{h}{2}\right)^3\cdot(1-\cos(\theta_A))^2} + \frac{12\cdot\mu\cdot B\cdot U\cdot h^2}{\left(B-\frac{h}{2}\right)^2\cdot(1-\cos(\theta_A))^2} - \gamma_{lv}\cdot c\cdot\frac{\pi}{2} \times\left[\frac{[\sin(\Delta-\theta_A)-\sin(\theta_A)]}{(\Delta-\pi)} + \frac{[\sin(\Delta-\theta_A)-\sin(\theta_A)]}{(\Delta+\pi)}\right] = 0 \quad (1)$$

The other symbols are also shown in Fig. 3 and defined in 'Nomenclature' section. This relationship shows the strong dependence of droplet contact angle hysteresis and deformation, Δ, on the flow channel velocity, U.

Channel/land masked images of the low flow rate (upper image) and high flow rate (lower image) are shown in Fig. 4. The images on the left side only show the liquid water in, or under, the channels. The images on the right side of Fig. 4 show the liquid water under the landings in diffusion media. These masking images also indicate the increase in channel water removal with flow rate, since the decrease in channel water is almost three times that of under landings ($\Delta W_1 > \Delta W_2$), between the low flow rate and high flow rate condition. Another important conclusion is that in both flow rate conditions, the water accumulation under the landings is more than that of channels. This implies that water easily accumulates under the landings, and it is difficult to remove from these locations for this parallel flow field. A possible reason for this is high heat removal rate through the landings (~80%) compared to moist air and hydrogen flowing in the channels (~20%).

At each test condition, in addition to the neutron images, the cell voltage data were taken in order to acquire the relation between the water accumulation in the cell and the performance. In Fig. 5, the cell performance and water mass at each test condition is plotted against the cathode gas flow rate. As observed, there is a peak value at low flow rate condition ~400 sccm, followed by a decrease in the water content with increasing flow rate, due to increased shear forces in the channel.

There appears to be two distinct regions in the cell performance depending on the flow rate. In Region 1, the cell performance is relatively low. In Region 2, with increasing flow rate, significant improvement is observed in the cell performance for both humidified and non-humidified conditions. In Region 1, water mass values of both humidified and non-humidified conditions are close to each other. However, cell performance is highly dependent on anode humidity [32], therefore the migration of water from the anode to the cathode side in the dry case, could cause anode dry-out and decrease the performance. The flow rate is increased in Region 2. This will have two important

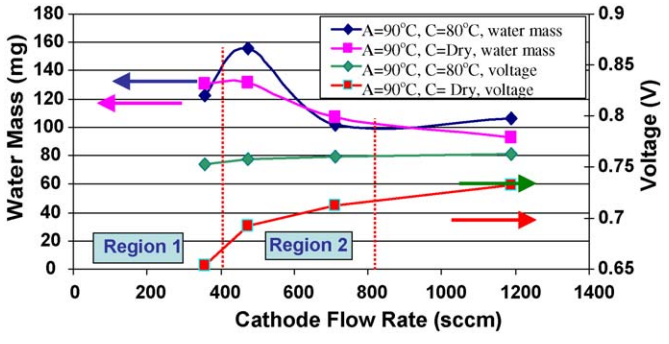

Fig. 5. Cell performance data and total water mass values vs. flow rate. Conditions 1–8 of Table 1. Current density at all conditions is 0.35 A cm^{-2}.

Table 3
Humidity and oxygen mole fraction calculations

Test condition	Anode flow (sccm)	Cathode flow (sccm)	RH_{in}[a] (%)	RH_{out}[a] (%)	$y_{O_2,in}$ (%)	$y_{O_2,out}$[b] (%)
1	149	356	115.5	140.9	16.1	11.3
2	199	475	115.5	134.4	16.1	12.3
3	299	712	115.5	128.0	16.1	13.3
4	497	1188	115.5	123.0	16.1	14.1
5	149	356	57.5	86.0	21.0	13.4
6	199	475	57.5	78.7	21.0	14.6
7	299	712	57.5	71.5	21.0	15.8
8	497	1188	57.5	65.9	21.0	16.7

[a] Anode and cathode considered together.
[b] Assuming anode and cathode have same water mole fraction.

consequences which will improve the cell performance significantly; decreased channel level liquid water mass and increased average oxygen concentration. The former effect will reduce the flooding problem in the cell and the latter one will increase the diffusion rate of the reactants due to the increased average oxygen mole fraction in the flow channels. Therefore, cell performance improves in this region. In Table 3, the fuel cell inlet and outlet oxygen mole fractions were calculated together with the corresponding relative humidities. It should be noted that, in the calculations anode and cathode flow is considered together to provide a metric of overall fuel cell saturation level.

Table 4 shows the increase in average oxygen mole fraction in the cell at elevated flow rate value. Note that the calculations showing greater than 100% relative humidity in Tables 3 and 4 are simply theoretical, and in practice means that condensation occurs.

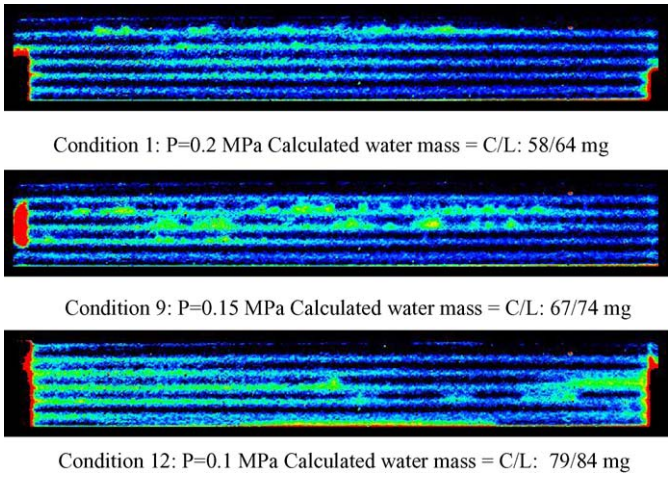

Fig. 6. Comparison of liquid water distribution at different cell pressures. Current density at all conditions is 0.35 A cm^{-2}.

3.2. Pressure effect

The second parameter investigated in this study was the cell pressure. Three different operating pressures were compared with each other in order to obtain an understanding of the pressure effect on water accumulation in the fuel cell. The images shown in Fig. 6 are in a decreasing pressure order, i.e. from 0.2 MPa to 0.1 MPa. In all images of Fig. 6, the flow rates are the same (anode/cathode: 149 sccm/356 sccm). Furthermore, at each condition, the anode flow is over humidified and cathode flow is fully humidifed. From Fig. 6, it can be seen that there is more liquid water in the cell at low cell pressure. Since these are the low flow rate conditions, there was a significant amount of channel level water in the cell.

At these over-humidified inlet operating conditions, decreasing the cell pressure favors water accumulation in the cell. The effect of the cell pressure is related to water accumulation

Table 4
Total relative humidity and inlet water vapor mole fraction in the fuel cell at different pressure conditions

Test conditions	Cathode flow (sccm)	RH_{in}[a] (%)	RH_{out}[a] (%)	$y_{O_2,in}$	$y^{sat}_{H_2O}$
Pressure: 0.2 MPa					
1	356	115.5	140.9	0.27	0.24
3	712	115.5	128.0	0.27	0.24
4	1188	115.5	123.0	0.27	0.24
Pressure: 0.15 MPa					
9	356	116.4	133.6	0.37	0.31
10	712	116.4	124.9	0.37	0.31
11	2376	116.4	118.9	0.37	0.31
Pressure: 0.1 MPa					
12	356	119.7	128.2	0.56	0.47
13	712	119.7	123.9	0.56	0.47
14	2376	119.7	121.0	0.56	0.47

[a] Anode and cathode considered together.

through inlet gas velocity. At a given constant inlet gas flow rate, flow velocity and density can be related to the mass flow rate:

$$\dot{m} = \rho \cdot A \cdot U \tag{2}$$

where density of the gas-phase flow at the inlet can be found using ideal gas equation, Eq. (3):

$$\rho = \frac{P_{\text{cell}} \text{MW}_{\text{mix}}}{R_{\text{u}} \cdot T_{\text{cell}}} \tag{3}$$

Therefore, the flow velocity must increase with decreasing cell pressure in order to keep the mass flow rate constant. This relation is important in terms of water removal from the channel since the shear force exerted on the droplets will grow with increasing velocity, as shown in Eq. (1). From this perspective, we would expect the water retained in the cell to decrease with decreasing pressure due to enhanced shear force enabled removal. However, the experimental results show an increase in liquid water content in the fuel cell with decreasing pressure. There is another factor affecting the pressure and water build-up in the fuel cell, namely, the humidity of the inlet flow. In these conditions, the cathode side was fully humidified and anode side was over humidified. In order to understand the effect of humidity on pressure, the overall (anode and cathode side together) humidity of the cell for these three conditions, shown in Table 4, was studied. For all the conditions, the overall inlet relative humidity was above 100%, indicating some condensation of the inlet flow will occur when entering the fuel cell. The amount of the condensed vapor is closely related to the cell pressure. At a given overall inlet relative humidity value, the amount of water vapor that inlet flow can maintain is given with Eq. (4):

$$y^*_{\text{H}_2\text{O}} = \left(\frac{P_{\text{sat}}}{P_{\text{cell}}}\right) \cdot \text{RH}^*_{\text{in}} \tag{4}$$

where RH^*_{in} is the total inlet relative humidity, given in Table 4, considering both the anode and cathode flows. At saturation conditions, the mole fraction of water vapor is:

$$y^{\text{sat}}_{\text{H}_2\text{O}} = \frac{P_{\text{sat}}}{P_{\text{cell}}} \tag{5}$$

using Eq. (5) and the ideal gas law, the amount of water vapor at the inlet and at the saturation conditions can be determined from Eq. (6):

$$\dot{n}_{\text{H}_2\text{O}} = \frac{(y^{\text{sat}}_{\text{H}_2\text{O}})(\dot{n}^{\text{dry}}_{\text{H}_2} + \dot{n}^{\text{dry}}_{\text{air}})}{1 - y^{\text{sat}}_{\text{H}_2\text{O}}} \tag{6}$$

The difference between the inlet and saturation water vapor amounts is equal to the number of moles of condensed water in the cell. In Table 5, the calculated amount of liquid water condensed in the cell due to the over-humidified inlet stream is shown for each pressure condition. It is seen that decreasing the cell pressure increases the liquid condensation in the cell and yields higher liquid water mass values. For the 0.2 MPa case, the condensing liquid water mass rate at the cell inlet is ~1.6 mg s^{-1} whereas in 0.1 MPa condition, this value increased by an order of magnitude to ~19 mg s^{-1}. Therefore, there is ~17 mg s^{-1} more liquid water condensation in lower pressure case resulting in a difference in calculated steady-state water mass values between the two pressure conditions of 40 mg, as observed in the neutron imaging experiments. For these over-humidified operating conditions, it is concluded that the liquid water in the cell increases with decreasing pressure.

Table 5
Amount of liquid water condensed at the cell inlet and exit due to the over-humidified gas flow

Test conditions	Cathode flow (sccm)	$\dot{n}^*_{\text{liquid,in}}$ (mol s^{-1})	$\dot{n}^*_{\text{liquid,out}}$ (mol s^{-1})
Pressure: 0.2 MPa			
1	356	2.59×10^{-5}	5.23×10^{-5}
3	712	5.17×10^{-5}	7.81×10^{-5}
4	1188	8.68×10^{-5}	1.13×10^{-4}
Pressure: 0.15 MPa			
9	356	4.42×10^{-5}	7.06×10^{-5}
10	712	8.85×10^{-5}	1.15×10^{-4}
11	2376	2.95×10^{-4}	3.21×10^{-4}
Pressure: 0.1 MPa			
12	356	1.50×10^{-4}	1.77×10^{-4}
13	712	3.01×10^{-4}	3.27×10^{-4}
14	2376	1.00×10^{-3}	1.03×10^{-3}

A similar trend is also reported in literature. Baschuk and Li [18] developed a model for two-phase flow in the fuel cell and calculated the degree of flooding at different pressure and humidity conditions. Their results show that at under-humidified conditions, increasing pressure yielded polarization losses at early stages of the performance curve whereas at high humidities, the phenomenon was reversed. In addition, the relation of pressure and water accumulation was studied in Yi et al. [33], and they concluded that a higher exit pressure was preferred to allow a higher exhaust dew point.

The voltage data at each condition were also taken in order to analyze the effect of cell pressure on the performance. In Fig. 7, the cell voltage data, together with the total water mass values, are plotted at each flow rate condition. The water amount in the cell decreases with increasing flow rate, which is consistent with the previous results. Consequently, a significant improvement in the cell performance (~60 mV) is observed at elevated flow rate

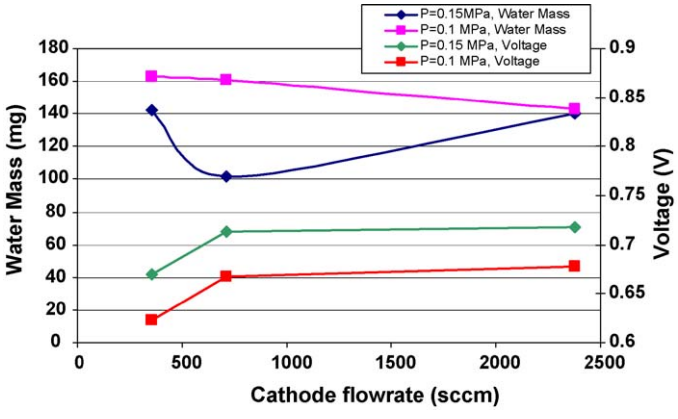

Fig. 7. Cell performance and total water mass for Conditions 9–14 of Table 1. Current density at all conditions is 0.35 A cm^{-2}.

values. Since the anode side is over humidified and cathode side is fully humidified, there is a high tendency of flooding in the fuel cell. A decrease in water amount will reduce the level of flooding in the cell and therefore will result in significant improvement in the performance as observed from the performance curves. In addition to the flooding effect, the oxygen mole fraction at the cathode side will be reduced at low pressure operation due to increased water vapor mole fraction at the inlet flow, and subsequent performance losses in the fuel cell attributed to the limatiton of reactant diffusion to the catalyst surface. These two effects yield lower performance at low operating pressure.

3.3. Inlet relative humidity effect

The last effect investigated in this study was the inlet relative humidity. Nine different tests were performed at three distinct overall humidification levels, 25%, 41% and 66%. The water accumulation and cell performance at each condition was analyzed to acquire understanding of the effect of reduced inlet humidity. The neutron images of each relative humidity condition are shown in Fig. 8. Note that all the other operating conditions besides inlet humidity were the same for the images in Fig. 8. The segregation of liquid water accumulation under the landings and in, or under the channels is most evident in these images. Most of the water accumulated under the landings appears as dark blue regions and there is almost no liquid in the channels.

Steady-state water mass under the land and in or under the channels is shown in Fig. 9. The difference between the water mass values of each condition is very small, and it is not possible to identify the trend in the water accumulation with increasing flow rate. However, as it is seen from Fig. 10, there is a significant performance drop in the cell with decreasing humidity, indicating that humidity has a major effect on water balance and therefore cell performance, even though the change in water mass with decreasing humidity is not observable. Consequently, the amount of water change required to produce the performance limiting characteristic of the dry-out phenomenon is very small. This is different than flooding which requires substantially greater amounts of water to deleteriously affect performance [21].

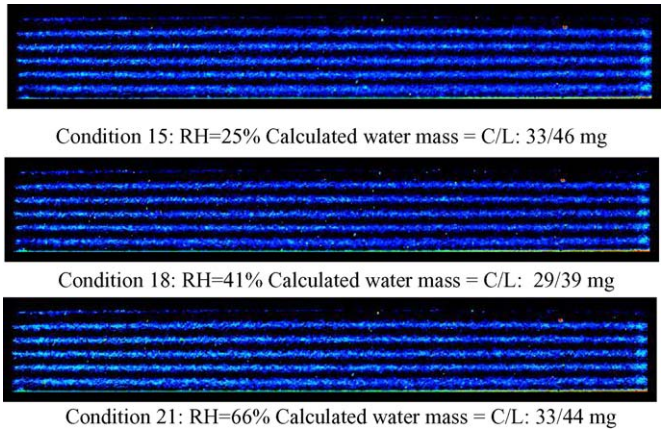

Fig. 8. Neutron images and total liquid water in the cell for different under humidified conditions. The liquid water amount in the cell is almost constant at each condition, although significant liquid water storage in steady state is still available. Current density at all conditions is 0.35 A cm^{-2}.

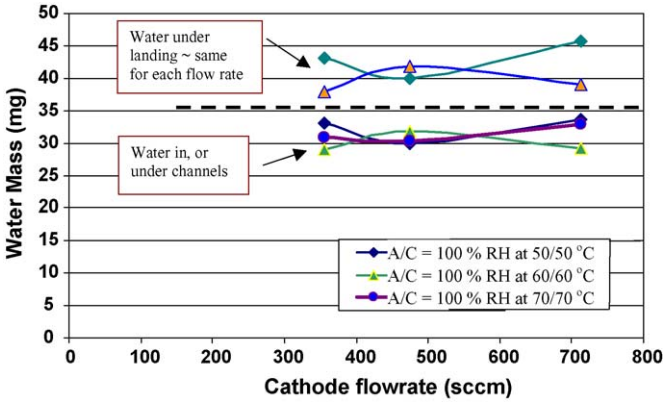

Fig. 9. Total liquid water mass values for the low humidity test Conditions 15–23 of Table 1. Current density at all conditions is 0.35 A cm^{-2}.

The membrane used in the experiments has a thickness of 40 μm with 2 g cm^{-3} density and 30% water uptake capacity by weight. Using these parameters, the maximum amount of water that the membrane can uptake is found by Eq. (7):

$$m^{\mathrm{el}}_{\mathrm{water}} = (A_{\mathrm{el}} \cdot \delta_{\mathrm{el}} \cdot \rho_{\mathrm{el}}) \cdot 0.3 \quad (7)$$

where electrolyte area is 14.56 cm^2. The maximum amount of water in the electrolyte calculated from this equation is 36 mg (2.42 mg cm^{-2}), which is equivalent to a thickness of 8 μm of liquid water. Incremental changes in the electrolyte water will result in significant differences in the cell performance through the ionic conductivity. Since the minimum detectable liquid water thickness with the existing neutron imaging system is 12.7 μm, the amount of water in the fuel cell appears to be constant with decreasing humidity even though there is a huge drop in the cell performance.

An important observation regarding the performance curves for each condition is that the performance versus flow rate relationship at under humidified conditions is opposite to that of fully humidified conditions. At fully humidified conditions, flood-

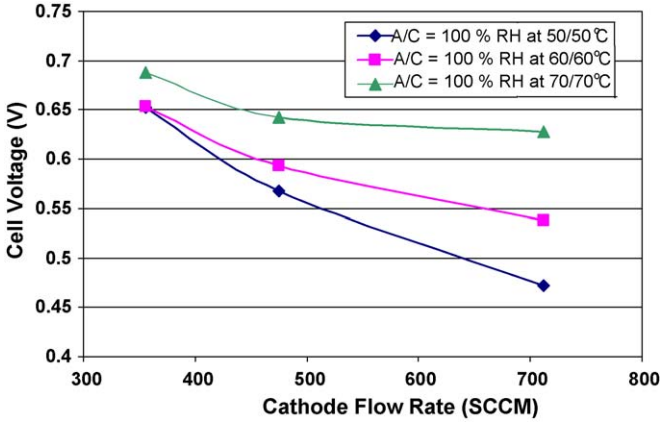

Fig. 10. Cell performance data for or the low humidity test Conditions 15–23 of Table 1. Current density at all conditions is 0.35 A cm^{-2}.

ing is the major factor determining the performance, therefore with higher water removal, i.e. higher flow rate, performance improves. On the contrary, at under humidifed operations, elevated flow rates enhances the electrolyte dry-out phenomena resulting significant performance losses.

4. Conclusions

The water management phenomena in polymer electrolyte fuel cells has a deterministic role in the cell performance and efficiency. In this study, the influence of fuel cell operation parameters on the liquid water storage and distribution was investigated through extensive experimental work. Test were conducted for three different parameters: inlet gas flow rate, cell pressure and inlet gas relative humidity. The results showed several important trends and conclusions. The liquid water accumulation in the fuel cell significantly decreases with increasing inlet gas flow rate. At low flow rate values, there was more liquid water in the cell and major part of it is accumulating in the flow channels. However, with increasing flow rate, a significant reduction in liquid water amount was observed, as slugs of liquid in the flow channels and some water under the lands were removed. Due to higher heat transfer and restricted mass transfer, locations under landings are liquid accumulation sites, and there was liquid water under the landings even at very high flow rates and low humidity. For over-humidified inlet conditions the amount of liquid water in the cell was found to be increasing with decreasing cell pressure, opposite the trend for underhumidified inlet conditions. The neutron images of under-humidifed conditions did not show a distinct difference in liquid water amounts, even though the cell performance at each case was significantly different from each other. This result indicated that the performance loss due to the electrolyte dry-out was a result of only a few miligrams in the 14.5 cm^2 active area cell, is consistent with electrode and/or membrane dry-out.

Acknowledgements

The authors wish to thank Dr. Kendra Sharp and Emin C. Kumbur for their contribution of Eq. (1) from ref. [26] and Dr. P.A. Chuang for his contribution in the experimental work.

References

[1] J. Larminie, A. Dicks, Fuel Cell Systems Explained, Wiley & Sons, Ltd., West Sussex, England, 2000, p. 61.
[2] A.Z. Weber, J. Newman, J. Electrochem. Soc. 150 (7) (2003) A1008–A1015.
[3] P. Choi, R. Datta, J. Electrochem. Soc. 150 (12) (2003) E601–E607.
[4] W.Y. Hsu, T.D. Gierke, J. Membr. Sci. 13 (3) (1982) 307–326.
[5] G.J.M. Janssen, M.L.J. Overvelde, J. Power Sources 101 (2001) 117–125.
[6] C. Kim, S. Lee, S. Srinivasan, J. Electrochem. Soc. 142 (8) (1995) 2670–2674.
[7] T. Fuller, J. Newman, J. Electrochem. Soc. 140 (5) (1993) 1218–1225.
[8] D.M. Bernardi, M.W. Verbrugge, J. Electrochem. Soc. 139 (9) (1992) 2477–2490.
[9] P. Berg, K. Promislow, J.S. Pierre, J. Stumper, B. Wetton, J. Electrochem. Soc. 151 (3) (2004) A341–A353.
[10] Z.H. Wang, C.Y. Wang, K.S. Chen, J. Power Sources 94 (2001) 40–50.
[11] P. Sridhar, R. Perumal, N. Rajalakshmi, M. Raja, K.S. Dhathathreyan, J. Power Sources 101 (2001) 72–78.
[12] M.M. Mench, Q.L. Dong, C.Y. Wang, J. Power Sources 124 (2003) 90–98.
[13] U. Pasaogullari, C.Y. Wang, Electrochim. Acta 49 (2004) 4359–4369.
[14] T.V. Nguyen, M.W. Knobbe, J. Power Sources 114 (2003) 70–79.
[15] N.P. Siegel, M.W. Ellis, D.J. Nelson, M.R. von Spakovsky, J. Power Sources 128 (2004) 173–184.
[16] M. Hu, X. Zhu, M. Wang, A. Gu, L. Yu, Energy Convers. Manage. 45 (2004) 1883–1916.
[17] F. Chen, Y.Z. Wen, H.S. Chu, W.M. Yan, C.Y. Soong, J. Power Sources 128 (2004) 125–134.
[18] C.C. Baschuk, X. Li, J. Power Sources 86 (2000) 181–196.
[19] A. Kumar, R.G. Reddy, J. Power Sources 113 (2003) 11–18.
[20] H. Ju, H. Meng, C.Y. Wang, Int. J. Heat Mass Transfer 48 (2005) 1303–1315.
[21] P.A. Chuang, A. Turhan, A.K. Heller, J.S. Brenizer, T.A. Trabold, M.M. Mench, Proceedings of the Third International Conference on Fuel Cell Science, Engineering and Technology, Paper #74051, 2005.
[22] K.S. Chen, M.A. Hickner, D.R. Noble, Int. J. Energy Res. 29 (2005) 1113–1132.
[23] K. Tüber, D. Pocza, C. Hebling, J. Power Sources 124 (2003) 403–414.
[24] H. Meng, X.G. Yang, K. Kinoshita, C.Y. Wang, Meeting Abstracts—206th Meeting of the Electrochemical Society, 2004.
[25] X.G. Yang, F.Y. Zhang, A.L. Lubawy, C.Y. Wang, Electrochem. Solid-State Lett. 7 (2004) A408–A411.
[26] E.C. Kumbur, K.V. Sharp, M.M. Mench, J. Power Sources, in press.
[27] R. Satijha, D.L. Jacobson, M. Arif, S.A. Werner, J. Power Sources 129 (2004) 238–245.
[28] A.B. Geiger, A. Tsudaka, E. Lehmann, P. Vontobel, A. Wokaun, G.G. Scherer, Fuel Cells 2 (2) (2002) 92–98.
[29] R.J. Bellows, M.Y. Lin, M. Arif, A.K. Thompson, D. Jacobson, J. Electrochem. Soc. 146 (3) (1999) 1099–1103.
[30] K. Mishima, T. Hibiki, H. Nishihara, Nucl. Eng. Des. 175 (1997) 25–35.
[31] N. Pekula, K. Heller, P.A. Chuang, A. Turhan, M.M. Mench, J.S. Brenizer, K. Ünlü, Nuclear Instruments and Methods in Physics Research Section A: Accelerators, Spectrometers, Detectors and Associated Equipment, 542, Issues 1–3, No. 21, 2005, pp. 134–141.
[32] Q. Dong, M.M. Mench, S. Cleghorn, U. Beuscher, J. Electrochem. Soc. 152 (2005) A2114–A2122.
[33] J.S. Yi, D. Yang, C. King, Am. Inst. Chem. Eng. AIChE J. 50 (2004) 2594–2603.